Theoretical and Applied Climatology (2020) 139:473–492
https://doi.org/10.1007/s00704-019-02973-y

ORIGINAL PAPER

Air temperature in Barcelona metropolitan region from MODIS satellite and GIS data

C. Serra[1] · X. Lana[1] · M. D. Martínez[1] · J. Roca[2] · B. Arellano[2] · R. Biere[2] · M. Moix[2] · A. Burgueño[3]

Received: 28 September 2018 / Accepted: 7 August 2019 / Published online: 31 August 2019

Abstract

The metropolitan region of Barcelona (BMR) is one of the most densely populated areas in the Mediterranean countries. The estimation of air temperature at a short scale from satellite measurements would contribute to a better understanding of the varied and complex spatial distribution of temperatures in BMR. This estimation would be a first step to study several patterns of the thermometric regime affecting population life quality and health. Taking advantage of MODIS data, air temperature measurements at 48 thermometric stations along the year 2015, together with their geographic and topographic data, multiple regression analyses have permitted to obtain fine spatial distributions (pixels of 1 km^2) of minimum, mean and maximum daily air temperatures. Previous to the multiple regression, Pearson coefficients and principal component analysis offer a first overview of the relevance of the variables on the empiric temperatures. The most relevant variables on the multiple regression process at annual and seasonal scale are land surface temperatures, latitude, longitude and calendar day. At a monthly scale, altitude (maximum temperature) and continentality (cold months for minimum and hot months for maximum temperatures) are also relevant. The best fits between empiric temperatures and those derived from the multiple regression processes have square regression coefficients within the range (0.92–0.96) for the annual case, (0.70–0.92) at seasonal scale and (0.52–0.87) at monthly scale. The root mean square error varies from 1.5 to 2.0 °C (annual case), from 1.3 to 2.0 °C (seasonal scale) and from 1.2 to 2.1 °C (monthly scale). In agreement with these regression coefficients and mean square errors, the obtained spatial distribution of temperatures is of notable quality. As an outstanding application, the detection of several urban heat islands on different conurbations within BMR along the Mediterranean coast becomes possible.

1 Introduction

The estimation of the land surface temperature (LST) from the thermal infrared radiation (TIR) emitted by the Earth became possible a few years after the arrival of remote sensing from the space. Rao (1972) was the first to apply TIR to estimate temperature patterns for the cities along the USA mid-Atlantic coast from data collected by the Improved TIROS Operational Satellite (Gallo et al. 1995). TIR measurement from the space permits to know the LST assigned to a pixel (Dash et al. 2001, 2002), without considering the multiple parts contained in this pixel, as vegetation, sunlit and shadowed soils, irregular urban surfaces or soil moisture, with different albedo and emissivity values (Tomlinson et al. 2011; Benali et al. 2012). In fact, TIR is derived from the top of atmosphere radiances, from which LST is obtained after applying corrections due to atmospheric attenuation, angular effects and emissivity values at the heterogeneous surface. Water vapour and aerosols are the main agents causing variable attenuation in the TIR signal. This reduces the LST availability to only under cloud-free conditions, to avoid a systematic bias toward colder-than-true values (Williamson et al. 2013). In this sense, the integration of synergistic information from satellite optical-IR and passive microwave remote sensing has been proved recently to permit consistent and reasonable temperature estimations with cloudy skies (Jang et al. 2014).

The right estimation of the temperature of the air at ≈ 2-m height above ground (T_a) from LST is possible but complex. The vertical lapse rate to be applied is function of the surface

✉ X. Lana
francisco.javier.lana@upc.edu

[1] Department of Physics, Technical University of Catalonia, Barcelona, Spain

[2] Department of Architectural Technology, Technical University of Catalonia, Barcelona, Spain

[3] Department of Applied Physics–Meteorology, University of Barcelona, Barcelona, Spain

energy balance, which varies in function of the nature of the surface and of the instant of the day, as also of advection, adiabatic processes, turbulence and latent heat fluxes, all of them affected by cloud cover, water vapour content and vegetation (Benali et al. 2012). During the night, the estimation of T_a becomes simpler because the earth surface behaves almost as homogeneous surface (Didari et al. 2017).

This T_a estimated from satellite measurements would solve the weather stations scarcity in wider regions, where the geospatial interpolation methods, as kriging or splines, cannot provide accurate estimations, as happens, for instance, in mountainous terrain (Lin et al. 2016) or undeveloped countries. In this way, T_a estimation becomes of crucial importance to solve spatial gaps for a wide range of applications, in such a way that it is accepted that TIR produces better T_a estimations than those obtained by interpolating ground-station temperatures (Mendelsohn et al. 2007).

In the first years of remote sensing, this strategy based on TIR permitted to obtain extended and automatic LST for large regions, but with a limited spatial resolution, as in the case of Meteosat satellite (e.g. Cresswell et al. 1999). Since the year 2000, the MODerate resolution Imaging Spectroradiometer (MODIS) sensor in Terra and Aqua polar satellites (http://modis.gsfc.nasa.gov/) have reduced the spatial resolution for LST to 1 km per pixel. In this way, two images per satellite per day are generated (Terra satellite passes daily over the equator close to 10:30 UTC and 22:30 UTC; Aqua at 13:30 UTC and 01:30 UTC), using both the 10.78–11.28 μm and 11.77–12.27 μm spectral bands, together with split-window algorithms (Wan et al. 2002). These MODIS products have been submitted to consistent validation (Coll et al. 2005; Wang et al. 2008). In addition to climatological applications, other biological and physical processes on the land and the ocean may be derived using 36 electromagnetic spectral bands from visible to TIR available from MODIS (Zhang et al. 2003; Wan et al. 2004; Wang et al. 2009) or also mapping the global distribution of urban land (Schneider et al. 2009).

Given the practical impossibility of T_a direct determination from MODIS Terra LST, different estimation methods have been applied (Zaksek and Schroedter-Homscheidt 2009). The simplest one consists in supposing a linear relation between T_a and LST by distinguishing different land cover types, as Shen and Leptoukh (2011) have applied to Central and Eastern Eurasia, or without this distinction for smaller regions (Fu et al. 2011; Sohrabinia et al. 2015). The consideration of the called temperature-vegetation index (TVX), proposed by Nemani and Running (1989), by applying the normalised difference vegetation index (NDVI) and ignoring its seasonal, ecosystem type and soil moisture variability, has permitted the inclusion of the vegetation cover as a relevant factor (Prihodko and Goward 1997; Vancutsem et al. 2010; Cristóbal et al. 2008; Nieto et al. 2011; Wenbin et al. 2013; Shah et al. 2013; Bustos and Meza 2015). Modifications have been also added, as the differential TVX method (Sun et al. 2014). Certainly, the vegetation cover is determinant by its transpiration cooling and latent heat fluxes, as also through their low albedo and roughness which aides efficient sensible heat dissipation (Benali et al. 2012). Alternatively, the multiple linear regression applies different variables in addition to LST and NVDI to estimate T_a, as latitude, distance from coast, altitude and solar radiation (Cristóbal et al. 2008) or albedo and solar radiation (Xu et al. 2014). Nevertheless, after having considered different predictors, Lin et al. (2012) have proved that just the altitude and LST permit to obtain T_a for East Africa. Zhang et al. (2011) also apply the solar declination variable along the year and LST to derive T_a in China. Kloog et al. (2017) derive daily T_a estimations from LST, NVDI, elevation and the grid cell percentage of urbanicity for France. But, in general, for extended regions, spatial-temporal variables as Julian day of the year, latitude, longitude, height above sea level, slope, curvature and distance to the coast use to be considered (Recondo et al. 2013; Peón et al. 2014; Good 2015; Thanh et al. 2016; Yang et al. 2017). A relation with the variables applied by different authors can be found in Janatian et al. (2017). Also, the use of spatio-temporal regression-kriging and incorporation of time-series of remote sensing images have been proved to permit significantly more accurate maps of temperature than if plain spatial techniques were used (Hengl et al. 2012). At the planetary scale, the new dataset of spatially interpolated monthly climate data for global land areas at a very high spatial resolution (approximately 1 km^2) has considered LST observations to cover areas with a low station density (Fick and Hijmans 2017). This effort improves the first LST map at the planetary scale from MODIS measures (Kilibarda et al. 2014).

Besides different valuable applications of the estimation of T_a from LST, this study should be the base of future detailed analyses of the urban heat island (UHI) of Barcelona considering its entire Metropolitan Region (BMR). Unless otherwise indicated, UHI intensity is derived as the difference in spatially averaged surface temperatures between urban and non-urbanised surroundings, as a measure of the excess of warmth of the urban atmosphere (Voogt and Oke 2003). UHI phenomenon has been usually analysed from air temperature measurements of a short number of gauges across the city, sometimes with emplacements submitted to criticism, as gardens or roofs, and others outside the city influence (Stewart 2011). This humble departing state (Landsberg 1981), due to the scarcity of points with measurements, has led to a first spatial and temporal characterisation of the phenomenon (Arnfield 2003). Later on, thermometers installed in automobile have permitted to extend the analysis for selected transects across the city (Caselles et al. 1991; Moreno-Garcia 1994) to derive a thinner description of the anomalous urban thermal behaviour in relation to the rural proximity of the city. Urban

networks of stations together with different rural temperature observatories around the city have been also undertaken permitting detailed descriptions (Giannaros and Melas 2012; Yang et al. 2013). The multiplicity of urban internal configurations, due to the diversity of geometry, morphology and size of the cities, together with local or regional air dynamics, as the mesoscale sea breeze in the case of littoral cities, makes the urban climate a difficult objective to be rightly modelled. This shortcoming is notably solved by considering T_a series derived from satellite remote sensing. Voogt and Oke (2003) have reviewed the research done with thermal remote sensing before MODIS application. They conclude that the complexity of the urban surface should be analysed through couple canopy radiative transfer models with both sensor view models and surface energy balance models to simulate air temperature in and above the urban canopy layer. With this purpose, Miao et al. (2009) have applied MODIS observations with dynamical models to simulate urban weather features for comparison with observations in Beijing. Nevertheless, most of the studies analyse the spatial UHI taking advantage of the high spatial resolution provided by MODIS but without considering air dynamics for single cities (Cheval et al. 2009; Cheval and Dumitrescu 2009; Fabrizi et al. 2011; Tomlinson et al. 2012; Ma et al. 2016), as also for sets of cities (Jin et al. 2005; Hung et al. 2006; Yasuoka 2006; Pongrácz et al. 2006, 2010; Imhoff et al. 2010), for selected episodes, months or a few years.

2 Database

2.1 Study area

The metropolitan region of Barcelona, BMR, with an extension of 3242.2 km^2 and a population density of 1566.2 inhabitants/km^2, according to IdesCat-2017 (*Institut Català d'Estadística*), is a crowded area close to the Mediterranean Sea. Particularly, Barcelona city, with a population of 1.6 million inhabitants, covers an area close to 100 km^2 with a population density close to 16,000 inhabitants/km^2. The orography of the analysed region is characterised by the Littoral and Pre-Littoral chains, with moderate altitudes up to 1700 m a.s.l., both parallel to the Mediterranean coast. Between both chains are placed the Vallès valley and Penedès Basin. The most extended urban area (Barcelona city) is constrained among the Mediterranean shoreline, the Littoral chain and Llobregat and Besós rivers. The main orographic features of the region and the distribution of altitude in meters are shown in Fig. 1a,b. Details of the spatial distribution of CORINE land cover classes (http://land.copernicus.eu/pan-european/corine-land-cover/clc-2012), at level 3 for the year 2012, are shown in Fig. 1c and Table 1.

2.2 Meteorological station data

Observed daily minimum, T_{min}; mean, T_{mean} and maximum, T_{max} temperatures are the dependent variables of this study. These come from 48 meteorological stations, 37 of them belonging to the *Servei Meteorològic de Catalunya* (www.meteocat.cat) and 11 to the *Agencia Estatal de Meteorología*, (www.aemet.es) for the year 2015. Data are obtained in both cases from automatic weather stations, and their quality is guaranteed by periodic instrumental controls of the two governmental institutions. Additionally, the 48 thermometric records are free of perturbations, such as sharp changes or artificial trends, in agreement with the results of the Buishand (1982) and Pettitt (1979) tests, as proposed by Wijngaard et al. (2003). Given that these possible perturbations cannot be detected analysing only 1 year, the two mentioned tests have been applied to longer records including the year 2015, and the results have been also compared with previous analysis of the thermometric regime in a wider area of Catalonia (Martínez et al. 2010). Figure 1 d shows the spatial distribution of the stations, where five of them are outside but very close to the studied region. The stations are well spread over BMR except in the north, where they are scarce. Table 2 gives the main geographical and topographic variables of the thermometric station emplacements. Figure 2 a and b show the histograms of altitudes for the 1 km^2 pixels covering all the BMA and for the set of meteorological stations respectively. Altitudes of the available thermometric stations are mostly emplaced below 600 m a.s.l.

2.3 Satellite data

The daily MOD11A1 LST measured by MODIS Terra, including daytime 10:30 UTC surface temperature, LST_d, and night time 22:30 UTC, LST_n, with 1 km^2 spatial resolution, has been used in this study. The normalised difference vegetation index, NDVI, is obtained from the 16-day MOD13Q1 product (with a resolution of 250 m):

$$NDVI = \frac{NIR - RED}{NIR + RED} \quad (1)$$

where NIR is the near-infrared reflectance band-2 (841–876 nm) and RED, the reflectance of the red band-1 (620–670 nm). The normalised difference build-up index, NDBI, is calculated as:

$$NDBI = \frac{MIR - NIR}{MIR + NIR} \quad (2)$$

where MIR is the surface reflectance band-6 (1628–1652 nm) from MOD09A1 product of 8-day average (with

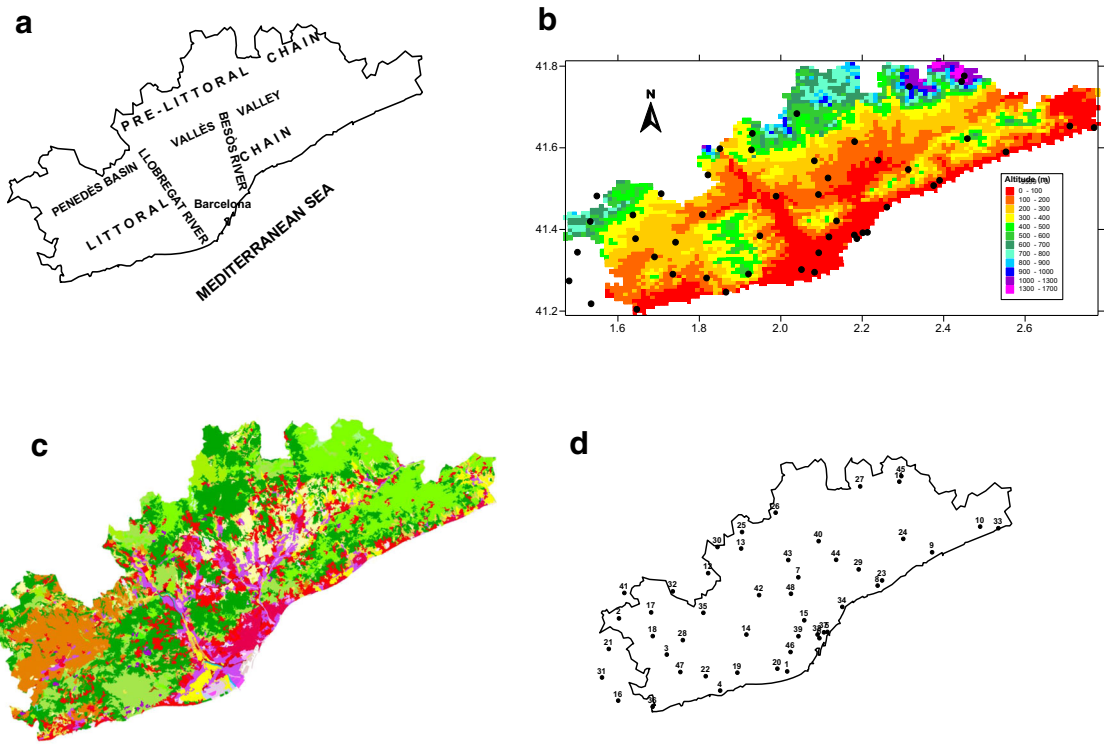

Fig. 1 Spatial distribution of main orographic features (**a**), altitude above sea level (**b**), CORINE land cover classes (**c**) and the thermometric stations (**d**)

a resolution of 500 m). Figure 2 c and d show the histograms of NDVI and NDBI for emplacements of temperature stations. A half of these coefficients are within the 0.3–0.5 interval, corresponding to emplacements with low vegetation cover. For the whole set of 1 km^2 pixels, the modal value of NDVI is shifted toward 0.6. In consequence, rural areas are slightly predominant in comparison with urban domains. With respect to NDBI, it is worth mentioning that most of the station emplacements have coefficients ranging from − 0.2 to 0.1. For the whole domain, the mode of NDBI is − 0.1, suggesting a slight predominance of nonurban areas.

2.4 GIS data and calendar day

Besides Satellite variables LST_d, LST_n, NDVI and NDBI, other six geographical and topographic variables are considered. These are latitude (lat), longitude (lon), distance to coast or continentality (con), altitude (alt), orientation (ori) and slope (slp) of the terrain for every meteorological station and pixel. The first three are derived from ArcGIS software (*Geographic Information Systems*, GIS). Altitude, orientation and slope are obtained from the Ground Digital Model (*MDT—Institut Cartogràfic I Geològic de Catalunya*, ICGC) with a 15 × 15 m^2 resolution. Table 3 summarises the minimum, mean and maximum of LST_d and LST_n, NDVI and NDBI, together with geographic and topographic variables. Furthermore, the calendar day, cd, has been transformed into a new calendar day, cd*, according to:

$$cd^* = \cos\frac{2\pi(cd - cd_{max})}{365} \tag{3}$$

to obtain the linearity respect to the air temperature (Janatian et al. 2017). cd_{max} is the calendar day for which the mean temperature along the year is the highest. Figure 3 a and b show the relationship between T_{mean} and cd or cd* respectively. cd_{max} for the year 2015 is equal to 200 (July 19th). Figure 3 b shows more signs of linearity between the air temperature and the transformed calendar day, cd*.

Figure 4 a shows the dependence of T_{max} on the orientation. This dependence is unclear and a linear relationship should be discarded. Trying to solve this lack of linearity, the orientation is given as sine and cosine compounds. Figure 4 b shows the case for T_{max} against sine compound, where a small linear increasing tendency is observed. Conversely, the cosine compound does not show signs of linear tendency.

3 Methodology

The estimation of surface air temperatures is based on the relationships between variables obtained from satellite (LSTd, LSTn, NDVI and NDBI), geographic and topographic data (latitude, longitude, altitude above sea level, orientation,

Table 1 Types of land cover (percentage and areas) on BMR

Land cover	Area (km^2)	(%)
Coniferous forest	866.91	26.7
Broad-leaved forest	493.41	15.2
Discontinuous urban fabric	333.53	10.3
Vineyards	293.50	9.0
Sclerophyllous vegetation	291.79	9.0
Non-irrigated arable land	173.43	5.3
Industrial or commercial units	166.17	5.1
Continuous urban fabric	132.75	4.1
Permanently irrigated land	95.16	2.9
Occupied by agriculture	68.76	2.1
Transitional woodland-shrub	68.26	2.1
Pastures	43.71	1.3
Complex cultivation patterns	36.72	1.1
Green urban areas	26.34	0.8
Mixed forest	22.44	0.7
Fruit trees and berry plantations	19.66	0.6
Sport and leisure facilities	19.48	0.6
Road and rail networks	18.54	0.6
Mineral extraction sites	14.05	0.4
Construction sites	9.34	0.3
Airports	9.33	0.3
Moors and heathland	8.35	0.3
Port areas	7.44	0.2
Olive groves	5.66	0.2
Beaches, dunes, sands	5.12	0.2
Salt marshes	4.22	0.1
Sparsely vegetated areas	3.45	0.1
Watercourses	3.37	0.1
Total	3244.72	100

slope and distance to coast), the modified calendar day (cd*) and empiric data (T_{min}, T_{mean} and T_{max}) recorded at the thermometric stations.

The first step consists of computing the Pearson correlation coefficient for all possible pairs of data, including empiric data. In this way, possible relationships between assumed independent variables can be detected. Additionally, the dependence of empiric data on the set of independent variables can be determined. The rotated principal component analysis (RPCA) (Jolliffe 1986; Richman 1986; Preisendorfer 1988) is the second step. In this way, more detailed characteristics of relationships between independent variables can be established; particularly, the ratio of data variance explained by every rotated principal component, RPC, and the contribution (factor loading) of every independent variable in the RPCs. These strategies, Pearson correlation and PCA, have been also applied by Thanh et al. (2016).

The third step consists of a multiple regression process with software from *Statistic package for Social Sciences*, *IBM-SPSS*, with an assumed linear relationship between empiric data and independent variables. The multiple regression goodness of fit is quantified by the square regression coefficient, R^2, including all the significant independent variables according to P values and $\alpha = 0.05$ (Harrell 2001) and by residuals between empirical, *emp*, and estimated, *est*, temperatures computed from the root mean square error, RMSE, and the mean average error, MAE. These errors are computed as:

$$RMSE = \left\{ N^{-1} \sum_{i=1}^{N} (emp_i - est_i)^2 \right\}^{1/2} \quad (4a)$$

$$MAE = \left\{ N^{-1} \sum_{i=1}^{N} |emp_i - est_i| \right\} \quad (4b)$$

The multiple regression process is repeated adding step by step a new independent variable. In this way, the relevance of every variable on the multiple regression process is contrasted by observing the changes in R^2 and RMSE. In addition to the coefficients of the multiple regression equations, the beta weights (standardised coefficients) are also computed to determine the relevance of every independent variable on the multiple regression equation.

As a summary, in comparison with other similar researches based on satellite and thermometric stations data, it should be mentioned that in this paper, first, cross-correlation and principal component analysis (PCA) permits the detection of possible redundant variables in the multiple regression process. Second, new geographic variables (orientation and slope) are tested. Third, both thermometric satellite data (LSTd and LSTn) are used in the multilinear regression, whatever minimum, T_{min}; mean, T_{mean} and maximum, T_{max}, daily temperatures are deduced from the multiple linear regression. It should be also remembered that only variables with absolute values of beta weight exceeding 0.01 have been finally considered for the multiple regression equations.

4 Results and discussion

4.1 Correlation coefficients and PCA

The Pearson correlation and the RPCA, based on the principal component analysis, PCA, have permitted to detect the degree of dependence between empiric data (T_{min}, T_{mean} and T_{max}) and the rest of parameters (geographic and topographic variables and data from a satellite). Table 4 shows the Pearson correlation coefficients among all variables. The high correlations, ranging from 0.86 to 0.97, between T_{min}, T_{mean} and T_{max} with daytime and nighttime LST and also with cd* are outstanding. The correlation of the empiric temperatures with the other parameters is always inside ± 0.23.

Table 2 GIS characteristics of the stations: longitude (Lon), latitude (Lat), altitude above sea level (Alt), distance to shoreline (Con), orientation of the slope (Ori) and topographic slope (Slp). Ori equal to − 1.0 indicates flat terrains (slope equal to 0.0)

	Station	Lon (°)	Lat (°)	Alt (m)	Con (m)	Ori (°)	Slp (%)
1	Barcelona—Airport	2.070000	41.292778	4	1802.41	− 1.00	0.00
2	Pontons	1.519167	41.416944	632	25,990.09	241.39	20.88
3	Vilafranca del Penedès	1.676944	41.330278	177	13,508.15	243.43	3.73
4	Sitges—Vallcarca	1.852500	41.243889	58	925.42	206.57	7.45
5	Barcelona—CMT	2.200000	41.390556	6	185.5	225.00	1.18
6	Barcelona—Drassanes	2.173889	41.375000	5	357.9	− 1.00	0.00
7	Sabadell—Aeródromo	2.103056	41.523611	146	14,686.96	− 1.00	0.00
8	Vilassar de Dalt	2.362500	41.505000	56	1586.01	150.95	8.58
9	Arenys de Mar	2.540000	41.587500	74	1406.52	71.57	5.27
10	Santa Susana	2.696944	41.650833	40	2814.06	158.20	8.98
11	Fontmartina	2.431111	41.760000	936	22,575.42	182.86	33.37
12	els Hostalets de Pierola	1.808131	41.531094	316	31,647.54	150.52	22.02
13	Vacarisses	1.914997	41.592518	343	31,910.67	90.00	11.67
14	Vallirana	1.935642	41.381968	252	13,153.66	160.35	24.78
15	Barcelona Observatori Fabra	2.123885	41.418432	411	6527.97	230.31	50.89
16	el Vendrell	1.521214	41.215534	59	3946.43	26.57	3.73
17	Font-rubí	1.623863	41.432921	415	25,729.52	161.57	7.91
18	Sant Martí Sarroca	1.630325	41.374910	257	19,374.48	90.00	3.33
19	PN del Garraf—el Rascler	1.907752	41.288317	573	3446.25	237.53	10.87
20	Viladecans	2.037870	41.299278	3	3275.54	− 1.00	0.00
21	el Montmell	1.487694	41.341706	545	18,210.02	153.43	3.73
22	Sant Pere de Ribes—Garraf	1.804796	41.278610	161	4823.22	199.80	22.14
23	Cabrils	2.377015	41.517731	81	2228.08	− 1.00	0.00
24	Dosrius—Montnegre Corredor	2.445317	41.619917	460	8362.11	209.74	13.44
25	Rellinars	1.917178	41.632863	421	34,368.7	315.00	9.43
26	Sant Llorenç Savall	2.026470	41.681290	528	31,792.68	155.56	10.07
27	Tagamanent—PN del Montseny	2.302911	41.747610	1030	26,303.64	221.82	21.25
28	la Granada	1.728574	41.366193	240	16,069.11	78.69	4.25
29	Vilanova del Vallès	2.300134	41.544401	126	7461.61	270.00	11.67
30	Montserrat—Sant Dimes	1.837509	41.595390	916	37,477.48	0.00	75.00
31	la Bisbal del Penedès	1.467169	41.271511	185	11,123.03	180.00	8.33
32	Canaletes	1.693370	41.485181	325	29,463.36	101.31	4.25
33	Malgrat de Mar	2.756574	41.647064	2	198.76	45.00	1.18
34	Badalona Museu	2.247574	41.452149	42	620.04	135.00	2.36
35	Sant Sadurní d'Anoia	1.794292	41.433861	164	21,985.71	65.56	20.14
36	Cunit	1.633462	41.201869	17	990.45	203.20	6.35
37	Barcelona Zoo	2.188469	41.389433	7	914.09	135.00	1.18
38	Barcelona—el Raval	2.167751	41.383899	33	1324.86	0.00	1.67
39	Barcelona Z. Universitària	2.105397	41.379197	79	5269.22	191.31	4.25
40	Caldes de Montbui	2.168358	41.612653	176	18,811	45.00	3.54
41	la Llacuna	1.535278	41.479475	589	32,688.25	165.96	6.87
42	Castellbisbal	1.975463	41.478924	147	20,531.47	71.57	15.81
43	Sabadell—Parc Agrari	2.069524	41.565680	258	19,910.4	135.00	3.54
44	Parets del Vallès	2.226185	41.567346	123	12,099.08	180.00	6.67
45	Puig Sesolles	2.437738	41.773622	1668	23,695.86	233.13	8.33
46	el Prat de Llobregat	2.080219	41.340456	8	5401.52	− 1.00	0.00
47	Canyelles	1.721949	41.288007	148	7951.78	21.80	8.98
48	Sant Cugat CAR	2.079558	41.483110	158	14,117.55	258.69	12.75

NDVI and NDBI are strongly correlated (− 0.79) as expected. There is also some correlation between these indices and the geographical variables latitude, longitude, altitude and slope, with values for NDVI between 0.26 and 0.52 and for NDBI between − 0.48 and − 0.36. It is important to mention that the correlations between the NDVI and NDBI indices with temperatures are low, with absolute values around 0.20. Latitude shows its highest correlation with longitude (0.62) and also with altitude (0.55), continentality (0.50), NDVI (0.48) and NDBI (− 0.48). Altitude has the highest correlation with continentality (0.60) and with latitude and NDVI index (0.52). The orientation has low correlations with all the other variables, although the highest ones correspond to those of the NDVI and NDBI indices. Finally, the slope, with low correlations in general, presents the highest ones with NDVI, NDBI, continentality and altitude.

Figure 5 shows some examples of the possible linear relationship between T_{min}, T_{mean} or T_{max} and some of the independent variables. The variables with the clearest linear relationship are, as expected, LST_d and LST_n according to the

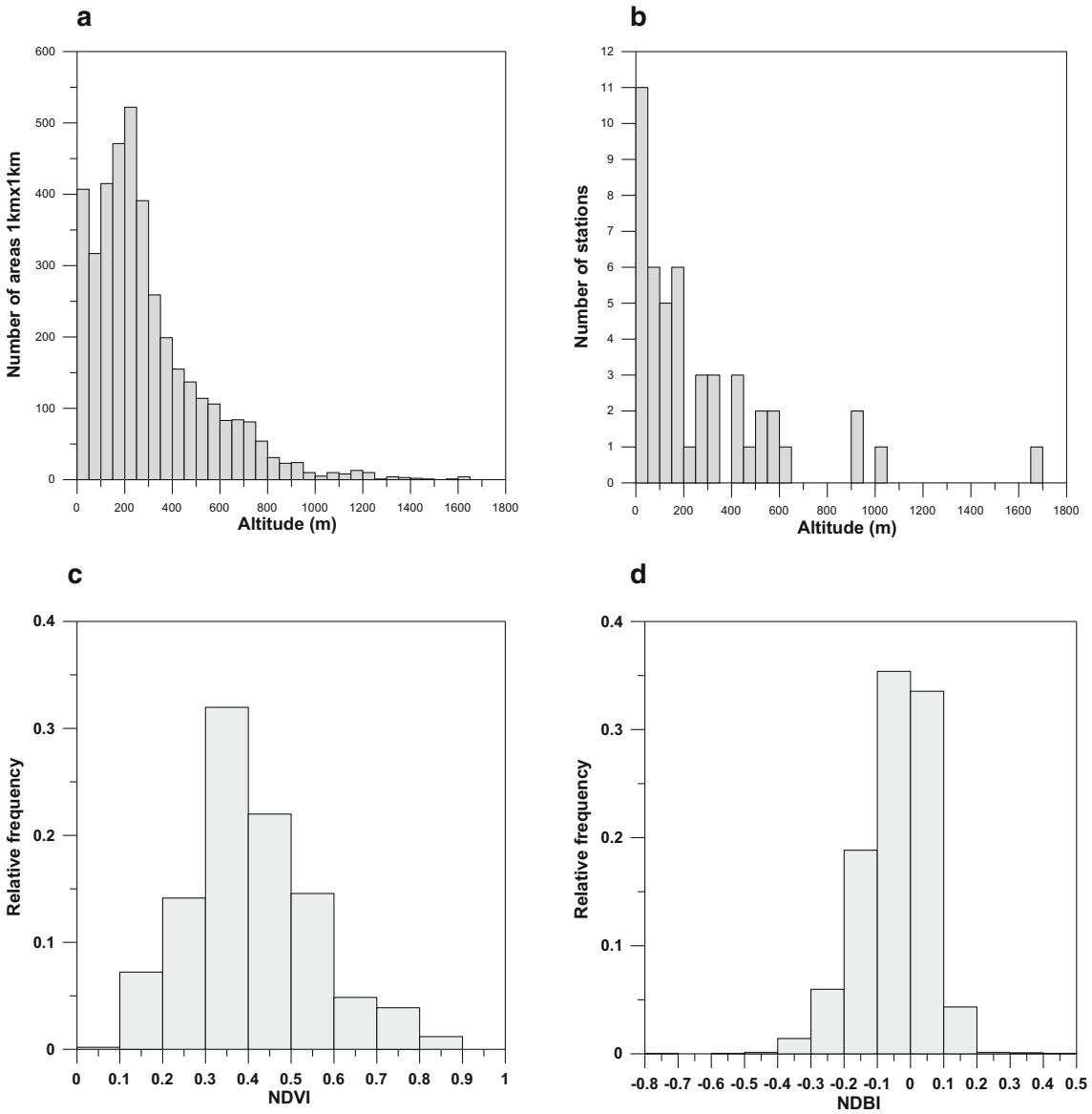

Fig. 2 Histograms of altitude for all the pixels (**a**) and meteorological stations (**b**). Histograms of NDVI (**c**) and NDBI (**d**) only for meteorological stations

high correlation value obtained between these variables and the temperatures.

The first four RPC selected with the eigenvalue exceeding 1.0 criterion have a similar percentage of explained variance (from 23.4 to 14.6%). Whereas they explain 77.2% of data variance, the remaining eight RPC are associated with the 22.8% of data variance. Consequently, the revision of the results offered by the PCA is centred on these four first RPCs. Tables 5b and 6b show the RPC factor loadings and the explained variance by the components, for the set of thermometric stations. The first component, RPC1, is strongly related to LST_d and LST_n and cd*, explaining 23.4% of data variance. The second component, RPC2, is mainly correlated with continentality and altitude, and also related to slope, latitude and NDVI. This component explains 22.6% of data variance. RPC3 is highly correlated with longitude and latitude, and slightly negative with NDBI. The third component explains 16.6% of data variance. Finally, RPC4 is notably correlated with the sine of the orientation, moderately with the cosine of the orientation and with NDVI and NDBI. This last component explains the variance of 14.6%. It is worth mentioning that NDVI and NDBI have middle weights on the second, third and fourth components, this fact suggesting that these two variables will probably have a lesser role in the multiple regression equations than expected. Given that PCA is applied to 12 variables for the 48 thermometric stations, this relatively low number of samples in comparison with the high number of 1 km^2 pixels could mask the relevance of some variables on the spatial distribution of T_{min}, T_{mean} and T_{max}. In order to detect these possible differences, RPCA has been also applied

Table 3 Mean, minimum and maximum of recorded diurnal (LSTd) and nocturnal (LSTn) temperatures, normalised difference vegetation index (NDVI) and normalised difference built-up index (NDBI), latitude (Lat), longitude (Lon), distance to shoreline (Con), altitude (Alt), orientation (Ori) and slope (Slp) for all 1 × 1 km pixels and for the 48 stations

	LSTd (°C)	LSTn (°C)	NDBI	NDVI	Lat (°)	Lon (°)	Con (m)	Alt (m)	Ori (°)	Slope (%)
Pixels										
Mean	23.00	11.09	− 0.09	0.52	41.52	2.09	15.565.01	294.53	165.86	23.40
Min	− 13.93	− 8.39	− 0.57	− 0.20	41.19	1.47	1.92	0.00	0.00	0.00
Max	48.13	30.65	1.00	0.98	41.81	2.78	41.103.86	1646.00	359.26	163.91
Station										
Mean	23.54	11.47	− 0.04	0.41	41.46	2.01	13.313.41	279.17	148.30	10.66
Min	− 3.35	− 5.67	− 0.75	0.10	41.20	1.47	185.50	2.00	0.00	0.00
Max	45.31	27.19	0.44	0.85	41.77	2.76	37.477.50	1668.00	360.00	75.00

to pixels with 1 km^2 resolution. Tables 5b and 6b summarise the RPC factor loadings and the explained variance by the components, for the 4042 pixels of 1 km^2. By comparing with results of Tables 5a and 6a, the first RPC is quite similar for both cases. The second RPC for Table 5a is equivalent to the third RPC for Table 5b, almost disappearing the contribution of the slope, NDVI and latitude. The third component (Table 5a), linked to latitude, longitude and NDBI, corresponds to the fourth RPC (Table 5b). The fourth RPC (Table 5a), with the contribution of NDVI, NDBI and orientation, is substituted by the fifth RPC (Table 5b), basically sinus of the orientation. Finally, the 2nd RPC (Table 5b) is constituted by NDBI, NDVI and slope. Conversely to Table 5a, where NDVI and NDBI are linked with moderate weights to more than one component, for Table 5b, these parameters are clearly related only to the second RPC. As a summary, the degrees of independence of the multiple regression variables are quite similar considering data from the set of thermometric stations or from a denser network of 1 km^2 pixels. Only some discrepancies are detected comparing factor loadings corresponding to NDVI and NDBI for both spatial resolutions.

4.2 Multiple regression

4.2.1 Annual case

The first multiple regression is applied to the annual case, including all days along the year 2015 accomplishing two conditions: first, only not cloudy days can be selected, given that LST_n, LST_d, NDVI and NDBI cannot be accurately computed for cloudy days; second, days with missing T_{min}, T_{mean} or T_{max} are not chosen for the multiple regression procedure. The set of days accomplishing both conditions are designed as *complete data days* and the same dataset with the same constraints are used at seasonal and monthly scale. Table 7 gives the different models obtained in every stepwise regression, being added one more variable until all the significant variables are used. This table also gives the R^2 coefficients and RMSE. The goodness of fit improves step by step, but with minor differences. For T_{min}, T_{mean} and T_{max} in the first step with a single variable, values of R^2 from 0.860 to 0.935 and RMSE from 1.8 to 2.7 °C are obtained. When all significant variables are involved, R^2 coefficients of 0.920, 0.955 and 0.918 and RMSE of 1.9 °C, 1.5 °C and 2.0 °C are reached.

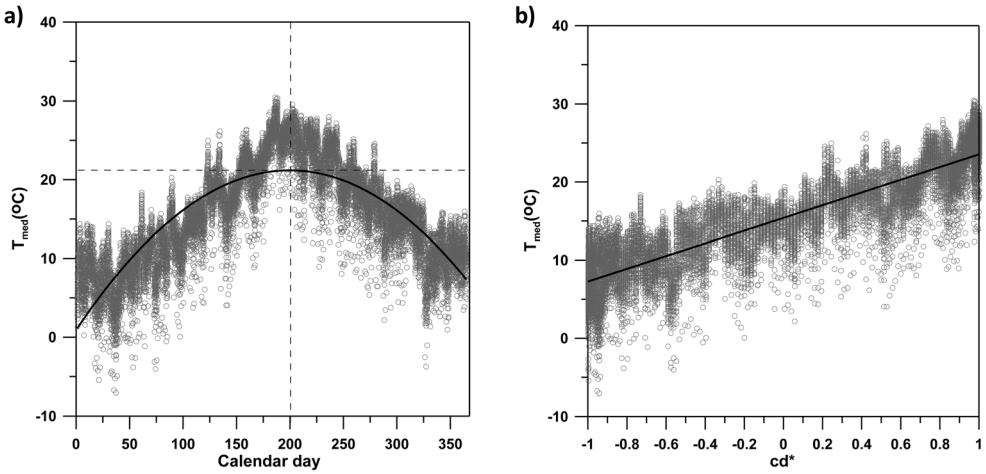

Fig. 3 Evolution of T_{mean} with the calendar day, cd (**a**) and the transformed calendar day, cd* (**b**)

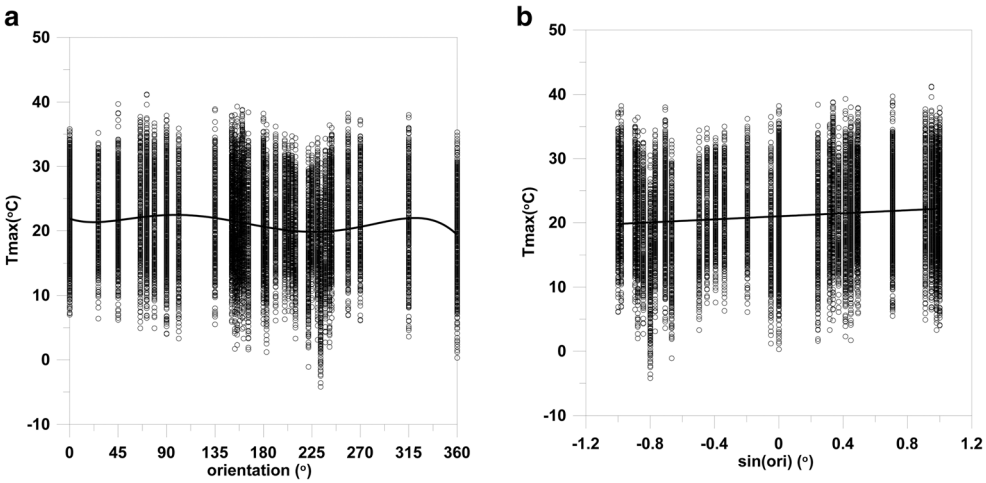

Fig. 4 Dependence of T_{max} on orientation, Ori (**a**) and sinus compound, ORI_{sin} (**b**)

Table 8 gives the standardised (beta weight) and non-standardised multiple regression coefficients for the last models of every dependent variable. In the case of T_{min}, the variable with the highest beta weight is LST_n, while LST_d does not appear in the multiple regression equation because it is not significant. Latitude, longitude and calendar day also have prominent standardised coefficients. For T_{mean}, the most important variables are LST_n and LST_d, with the rest of the variables having small or non-significant coefficients. Finally, in the case of T_{max}, the variables LST_d and LST_n have the highest beta weights and are also quite similar. Latitude, longitude and altitude also play a significant role in T_{max}. It should be noted that NDVI and NDBI indices have small or non-significant coefficients.

Orientation and slope are the variables that present the lowest beta weight coefficients for the three temperatures, possibly because a much denser network of stations would be necessary to represent all the variety of slopes and orientations. Figure 6 shows the bar histogram of the beta coefficients of the last model, including all the significant variables. It is outstanding the positive values for LST_n and, not so relevant, the positive values of LST_d. Among the negative values, the beta weight corresponding to latitude for T_{min} is the most relevant.

The relationships between the temperatures obtained from the multiple regression equations and the observed T_{min}, T_{mean} and T_{max} are plotted in Fig. 7. While R^2 for T_{mean} is 0.96, for T_{min} and T_{max} is 0.92. The RMSE (MAE) ranges from 1.5

Table 4 Pearson correlation coefficients for empiric temperature data, satellite data, geographic and topographic variables and transformed calendar day. The not significant coefficients ($\alpha = 0.05$) are codified as ns

	T_{max}	T_{mean}	T_{min}	LST_d	LST_n	NDBI	NDVI	Lat	Lon	Con	Alt	ori_{sin}	ori_{cos}	Slp	cd*
T_{max}	1000	0.961	0.881	0.928	0.913	0.214	−0.210	−0.127	−0.064	−0.071	−0.229	0.100	0.036	−0.112	0.868
T_{mean}	0.961	1000	0.968	0.930	0.967	0.194	−0.221	−0.139	ns	−0.162	−0.200	0.042	0.036	−0.079	0.897
T_{min}	0.881	0.968	1000	0.864	0.953	0.163	−0.205	−0.146	0.070	−0.227	−0.157	−0.018	0.036	−0.035	0.874
LST_d	0.928	0.930	0.864	1000	0.907	0.247	−0.262	−0.143	−0.043	−0.113	−0.204	0.066	0.060	−0.145	0.855
LST_n	0.913	0.967	0.953	0.907	1000	0.139	−0.181	−0.102	0.087	−0.203	−0.166	ns	0.039	−0.060	0.902
NDBI	0.214	0.194	0.163	0.247	0.139	1000	−0.792	−0.482	−0.463	−0.066	−0.379	0.269	0.257	−0.357	0.136
NDVI	−0.210	−0.221	−0.205	−0.262	−0.181	−0.792	1000	0.481	0.255	0.281	0.524	−0.300	−0.291	0.445	−0.103
lat	−0.127	−0.139	−0.146	−0.143	−0.102	−0.482	0.481	1000	0.624	0.502	0.551	0.037	−0.028	0.242	ns
lon	−0.064	ns	0.070	−0.043	0.087	−0.463	0.255	0.624	1000	−0.331	0.034	−0.110	ns	−0.011	ns
con	−0.071	−0.162	−0.227	−0.113	−0.203	−0.066	0.281	0.502	−0.331	1000	0.599	0.182	0.037	0.369	ns
alt	−0.229	−0.200	−0.157	−0.204	−0.166	−0.379	0.524	0.551	0.034	0.599	1000	−0.281	−0.177	0.435	ns
ori_{sin}	0.100	0.042	−0.018	0.066	ns	0.269	−0.300	0.037	−0.110	0.182	−0.281	1000	0.210	−0.187	ns
ori_{cos}	0.036	0.036	0.036	0.060	ns	0.257	−0.291	−0.028	ns	0.037	−0.177	0.210	1000	ns	ns
slp	−0.112	−0.079	−0.035	−0.145	−0.060	−0.357	0.445	0.242	−0.011	0.369	0.435	−0.187	ns	1000	ns
cd*	0.868	0.897	0.874	0.855	0.902	0.136	−0.103	ns	ns	ns	ns	ns	ns	ns	1000

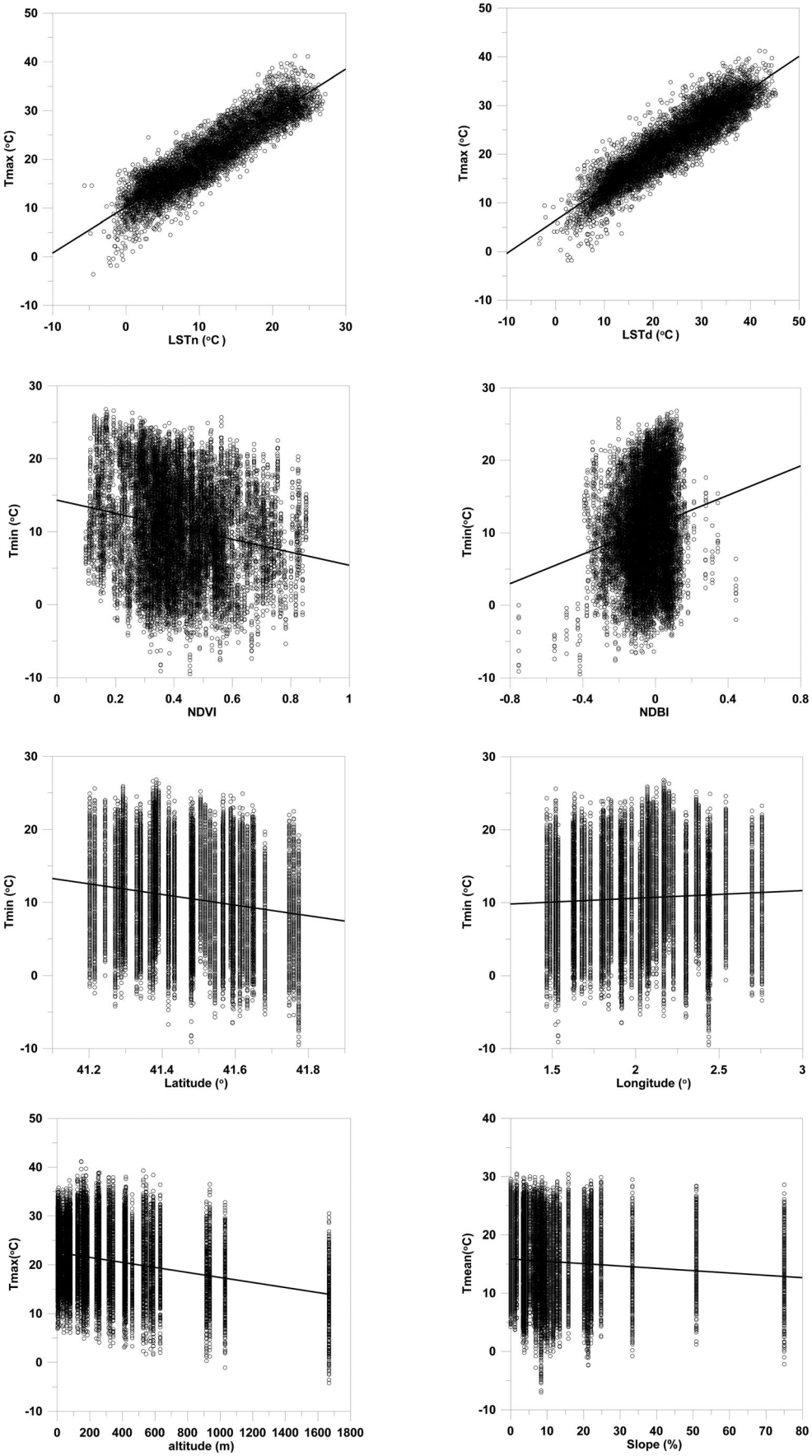

Fig. 5 Dependence of T_{max} and T_{min} on some of the variables of the multiple regression process

Table 5 Rotated principal components

	(a) RPC (stations)				(b) RPC (pixels)				
	1	2	3	4	1	2	3	4	5
LSTdia	0.962	−0.103	−0.070	0.088	0.957	−0.194	−0.036	−0.036	0.001
LSTnit	0.964	−0.131	0.031	−0.022	0.969	−0.025	−0.102	0.014	0.000
NDBI	0.137	−0.343	−0.558	0.546	0.156	−0.851	−0.033	−0.306	0.055
NDVI	−0.136	0.552	0.388	−0.544	−0.153	0.878	0.160	0.245	−0.046
Lat	−0.036	0.531	0.784	0.127	0.018	0.232	−0.300	0.899	−0.022
Lon	0.032	−0.228	0.933	−0.098	−0.020	0.248	0.439	0.819	0.002
Con	−0.067	0.897	−0.083	0.283	−0.047	0.045	0.946	−0.016	0.025
Alt	−0.067	0.817	0.152	−0.224	−0.035	0.457	0.769	0.061	−0.016
Slp	−0.030	0.664	0.000	−0.255	0.015	0.789	0.170	−0.058	0.035
ori_{sin}	−0.012	−0.099	0.073	0.777	0.010	0.073	−0.069	−0.096	0.932
ori_{cos}	0.009	0.012	−0.065	0.570	0.022	0.224	−0.167	−0.291	−0.378
cd*	0.978	0.046	−0.019	0.009	0.977	−0.028	0.043	−0.002	−0.004

(a) 48 thermometric stations

(b) 4042 pixels of 1 km × 1 km

(1.2) °C for T_{mean} to 2.0 (1.6) °C for T_{max}. The histogram for T_{mean} residuals is also shown in this figure. Fifty-one per cent of differences between estimated and observed temperatures are lower or equal to 1.0 °C.

4.2.2 Seasonal and monthly cases

Table 9 shows the R^2, RMSE and the number of samples, N, with complete data for seasonal multiple regressions and for the different temperatures. The highest correlations correspond to T_{mean} for spring and autumn, possibly due to the moderate range of the temperatures in these seasons. The lowest R^2 corresponds to the winter T_{min}. The RMSE values do not exceed 2.0 °C, which corresponds to T_{max} in summer.

The standardised beta coefficients for each variable are given in Table 10, with only significant coefficients. The italic entries correspond to coefficients greater than 0.10, seeing at a glance the most important variables in the multiple regression equations. T_{mean} is the variable that depends on the minimum number of variables in any season of the year, especially in spring and autumn. For example, in autumn, only the LST_n and LST_d temperatures have notable beta coefficients, and in spring, the cd* is also important. The NDVI and NDBI indices do not have high coefficients in any of the seasons. Only NDVI has values slightly higher than 0.10 in winter and summer for T_{max}, while NDBI has a negative coefficient in spring for T_{max}. The geographical variables that more contribute to the multiple regression are latitude, longitude, continentality and altitude, especially for T_{max} and T_{min}. Slope and orientation have small or non-significant beta weights.

Table 11 shows R^2, RMSE and N for every monthly multiple regression and for each temperature. For monthly cases, R^2 is lower than for seasonal or annual cases, ranging from 0.503 for July (T_{max}) to 0.867 for November (T_{mean}). However, RMSE have lower values than seasonal or annual cases, especially for T_{mean}, which ranges from 1.2 to 1.5 °C. The highest values correspond to April (T_{min}) and July (T_{max}), both with 2.1 °C. Figure 8 shows the RMSE for every month and Fig. 9 the estimated versus observed T_{mean} for November. Table 12 summarises the significant variables on the multiple regression process for every month and the different temperatures. A significant difference in comparison with annual and seasonal scale is the relevance of LST. Whereas LST is the most relevant at annual and seasonal scales, some differences are detected at monthly scale depending on the specific month and T_{min}, T_{mean} and T_{max}. The first multiple regression

Table 6 Total variance and percentage of variance and cumulated variance for every RPC

RPC (a)	Total	Variance (%)	Cumulated (%)	RPC (b)	Total	Variance (%)	Cumulated (%)
1	2811	23,427	23,427	1	2862	23,849	23,849
2	2712	22,600	46,027	2	2539	21,158	45,006
3	1992	16,600	62,627	3	1872	15,599	60,606
4	1753	14,606	77,232	4	1736	14,470	75,076
				5	1019	8492	83,568

(a) 48 thermometric stations. (b) 4042 pixels of 1 km × 1 km

Table 7 Models obtained with the stepwise regression analysis for T_{min}, T_{mean} and T_{max} at annual scale

	R^2	RMSE	Variables
Model T_{min}			
1	0.908	2075	LSTn
2	0.910	2047	LSTn, lat
3	0.912	2027	LSTn, lat, cd
4	0.914	2004	LSTn, lat, cd, lon
5	0.916	1981	LSTn, lat, cd, lon, slp
6	0.917	1968	LSTn, lat, cd, lon, slp, NDVI
7	0.919	1947	LSTn, lat, cd, lon, slp, NDVI, alt
8	0.920	1937	LSTn, lat, cd, lon, slp, NDVI, alt, ori_{sin}
9	0.920	1932	LSTn, lat, cd, lon, slp, NDVI, alt, ori_{sin}, con
10	0.920	1930	LSTn, lat, cd, lon, slp, NDVI, alt, ori_{sin}, con, NDBI
11	0.920	1928	LSTn, lat, cd, lon, slp, NDVI, alt, ori_{sin}, con, NDBI, ori_{cos}
Model T_{mean}			
1	.935	1780	LSTn
2	.950	1551	LSTn, LSTd
3	.952	1525	LSTn, LSTd, lon
4	.953	1509	LSTn, LSTd, lon, ori_{sin}
5	.954	1497	LSTn, LSTd, lon, ori_{sin}, cd
6	.955	1484	LSTn, LSTd, lon, ori_{sin}, cd, alt
7	.955	1480	LSTn, LSTd, lon, ori_{sin}, cd, alt, slp
8	.955	1474	LSTn, LSTd, lon, ori_{sin}, cd, alt, slp, ori_{cos}
Model T_{max}			
1	.861	2659	LSTd
2	.890	2365	LSTd, LSTn
3	.896	2299	LSTd, LSTn, lon
4	.900	2248	LSTd, LSTn, lon, ori_{sin}
5	.903	2222	LSTd, LSTn, lon, ori_{sin}, lat
6	.913	2096	LSTd, LSTn, lon, ori_{sin}, lat, alt
7	.916	2069	LSTd, LSTn, lon, lat, alt, NDVI
8	.917	2053	LSTd, LSTn, lon, lat, alt, NDVI, cd
9	.918	2046	LSTd, LSTn, lon, lat, alt, NDVI, cd, ori_{cos}
10	.918	2044	LSTd, LSTn, lon, lat, alt, NDVI, cd, ori_{cos}, ori_{sin}
11	.918	2042	LSTd, LSTn, lon, lat, alt, NDVI, cd, ori_{cos}, ori_{sin},con
12	.918	2041	LSTd, LSTn, lon, lat, alt, NDVI, cd, ori_{cos}, ori_{sin},con, slp

Table 8 Standardised and not standardised multiple linear regression coefficients for the annual case. Discarded variables for the multiple regression are codified by *ns*

	Standardised coefficients			Coefficients		
	T_{min}	T_{mean}	T_{max}	T_{min}	T_{mean}	T_{max}
Constant				532.394	5.023	− 228.921
LST_d	ns	0.245	0.414	ns	0.172	0.298
LST_n	0.801	0.660	0.473	0.786	0.660	0.484
NDBI	0.027	ns	ns	1.818	ns	ns
NDVI	− 0.031	ns	0.057	− 1.481	ns	2.812
lat	− 0.286	ns	0.123	− 13.089	ns	5.886
lon	0.234	− 0.032	− 0.149	5.015	− 0.703	− 3.341
con	0.096	ns	0.062	5.723E−5	ns	3.839E−5
alt	0.083	− 0.043	− 0.189	0.002	− 0.001	− 0.004
ori_{sin}	0.033	0.029	0.015	0.368	0.326	0.178
ori_{cos}	− 0.016	− 0.020	− 0.028	− 0.175	− 0.221	− 0.315
slp	0.047	0.022	− 0.014	0.023	0.011	− 0.007
cd	0.144	0.092	0.091	1.398	0.914	0.921

variable for T_{min} is the latitude for 8 months, the longitude (1 month) and LST_n only for 3 months. Conversely, for T_{mean}, LST_n is the most relevant for 11 months. Only for August is detected a slightly higher relevance of LST_d in comparison with LST_n. Finally, for T_{max}, the first multiple regression variable is the altitude for 5 months, LST_d (5 months) and LST_n (2 months).

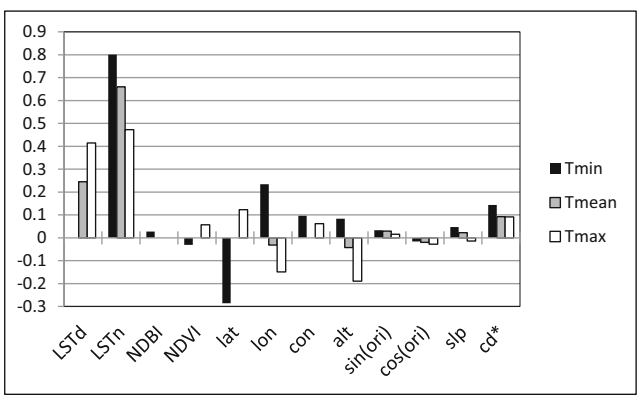

Fig. 6 Histogram of the beta coefficients of the last model at an annual scale for T_{min}, T_{mean} and T_{max}

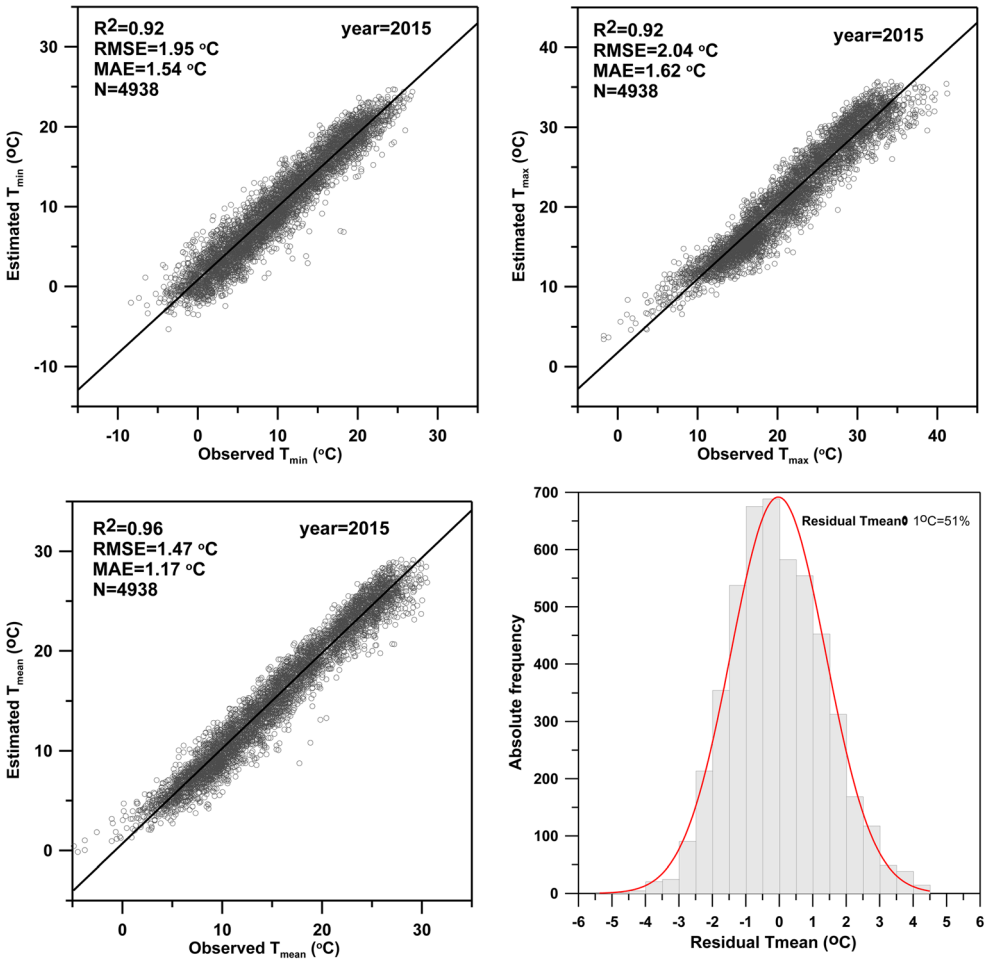

Fig. 7 Estimated versus observed T_{min}, T_{mean} and T_{max}, and the histogram for residual T_{mean} at an annual scale

4.3 Spatial distribution of T_{min}, T_{mean} and T_{max}

Some examples of the spatial distribution of temperatures on BMR obtained by multiple regression are shown in Figs. 10, 11, and 12. Figure 10 corresponds to T_{min}, T_{mean} and T_{max} obtained for November 29. The UHI phenomenon is quite evident for T_{min}, being associated with Barcelona city and a neighbouring area at the south of the city with the highest temperatures. Yellow, green and blue areas represent zones of lower temperatures, which correspond to the Littoral and Pre-Littoral chains (yellow and blue areas respectively) and the Vallès valley (green area). The combined effect of the vicinity to the Mediterranean coast and the UHI phenomenon is detected on the T_{mean} map, with the highest temperatures along a narrow littoral fringe. It is also worth mentioning the detection of two nuclei of high temperatures, spatially coincident with those observed for T_{min}. For T_{max}, this effect of the vicinity to the littoral disappears and high temperatures cover a good part of the metropolitan region. Only at the northern extreme of BMR (Pre-Littoral chain) small green and blue areas are detected with lower temperatures.

Table 9 Square regression coefficient, R^2, root mean square error, RMSE and number of samples, N, at seasonal scale

Season	Variable	R^2	RMSE	N
Winter	T_{min}	0.696	1.95	1241
	T_{mean}	0.853	1.32	1241
	T_{max}	0.799	1.83	1241
Spring	T_{min}	0.857	1.96	1368
	T_{mean}	0.921	1.35	1368
	T_{max}	0.852	1.94	1368
Summer	T_{min}	0.765	1.73	1146
	T_{mean}	0.829	1.42	1146
	T_{max}	0.738	1.97	1146
Autumn	T_{min}	0.808	1.83	1183
	T_{mean}	0.865	1.41	1183
	T_{max}	0.821	1.67	1183

At seasonal scale, some examples of the spatial distribution of average T_{min} for the winter season are shown in Fig. 11. Figure 12 depicts the monthly average of T_{min} for winter months (January, February and March). In spite of the spatial distributions, the other three seasons are obtained with a notable degree of accuracy; the winter case

Table 10 Standardised and not standardised multiple linear regression coefficients for the seasonal scale. Discarded variables for the multiple regression are codified by *ns*

	Winter			Spring			Summer			Autumn		
	T_{min}	T_{mean}	T_{max}	T_{min}	T_{mean}	T_{max}	T_{min}	T_{mean}	T_{max}	T_{min}	T_{mean}	T_{max}
LST_d	*0.277*	*0.457*	*0.643*	−0.055	*0.190*	*0.349*	0.061	*0.331*	*0.534*	*0.188*	*0.282*	*0.476*
LST_n	*0.641*	*0.625*	*0.409*	*0.712*	*0.611*	*0.458*	*0.497*	*0.301*	0.068	*0.709*	*0.663*	*0.452*
NDBI	ns	ns	0.062	ns	−0.053	*−0.114*	ns	ns	−0.074	ns	ns	ns
NDVI	−0.085	ns	*0.121*	−0.052	ns	ns	ns	ns	*0.120*	−0.077	−0.057	0.052
Lat	*−0.598*	ns	*0.334*	*−0.387*	ns	*0.104*	*−0.478*	ns	ns	*−0.623*	ns	*0.284*
Lon	*0.457*	ns	*−0.264*	*0.320*	ns	*−0.221*	*0.455*	ns	ns	*0.465*	ns	*−0.350*
Con	*0.305*	*0.115*	ns	*0.129*	ns	*0.167*	ns	ns	*0.201*	*0.256*	ns	ns
Alt	*0.128*	*−0.119*	*−0.412*	*0.101*	−0.088	*−0.206*	0.060	*−0.193*	*−0.323*	*0.237*	ns	*−0.390*
Slp	0.077	0.049	ns	0.063	ns	ns	*0.117*	0.061	ns	0.085	0.075	−0.036
ori_{sin}	0.064	ns	−0.038	0.039	0.044	0.065	0.043	0.056	0.067	0.059	0.036	ns
ori_{cos}	−0.052	−0.054	ns	ns	−0.021	−0.048	ns	−0.030	−0.064	ns	ns	ns
cd*	*−0.131*	*−0.138*	*−0.181*	*0.234*	*0.213*	*0.176*	*0.209*	*0.310*	*0.297*	ns	ns	−0.040

Table 11 Square regression coefficient, R^2, root mean square error, RMSE and number of samples, N, at monthly scale

Month	Variable	R^2	RMSE	N
January	T_{min}	0.671	1.86	609
	T_{mean}	0.815	1.24	609
	T_{max}	0.726	1.72	609
February	T_{min}	0.664	1.84	356
	T_{mean}	0.824	1.24	356
	T_{max}	0.774	1.72	356
March	T_{min}	0.707	1.96	276
	T_{mean}	0.824	1.34	276
	T_{max}	0.788	1.92	276
April	T_{min}	0.648	2.06	393
	T_{mean}	0.769	1.32	393
	T_{max}	0.692	1.68	393
May	T_{min}	0.517	1.77	455
	T_{mean}	0.651	1.20	455
	T_{max}	0.604	1.76	455
June	T_{min}	0.692	1.67	520
	T_{mean}	0.748	1.21	520
	T_{max}	0.605	1.90	520
July	T_{min}	0.606	1.66	504
	T_{mean}	0.606	1.29	504
	T_{max}	0.503	2.05	504
August	T_{min}	0.665	1.67	423
	T_{mean}	0.727	1.25	423
	T_{max}	0.666	1.60	423
September	T_{min}	0.735	1.51	219
	T_{mean}	0.779	1.22	219
	T_{max}	0.746	1.40	219
October	T_{min}	0.706	1.74	301
	T_{mean}	0.765	1.45	301
	T_{max}	0.797	1.40	301
November	T_{min}	0.825	1.81	615
	T_{mean}	0.867	1.37	615
	T_{max}	0.822	1.70	615
December	T_{min}	0.669	1.76	267
	T_{mean}	0.728	1.28	267
	T_{max}	0.721	1.22	267

for T_{min} is introduced here given that the characteristics of these four maps clearly manifest the UHI phenomenon in the BMR. The map of average winter T_{min} reproduces the two nuclei of UHI on the downtown of the Barcelona city and at the south along the coast. If the spatial analysis is revised at a monthly scale, very similar spatial patterns to those observed for November 29 (T_{min}) are now found for the cold months of January and February. In the case of March (a more temperate month), the UHI is not so clear, but the two nuclei appear again.

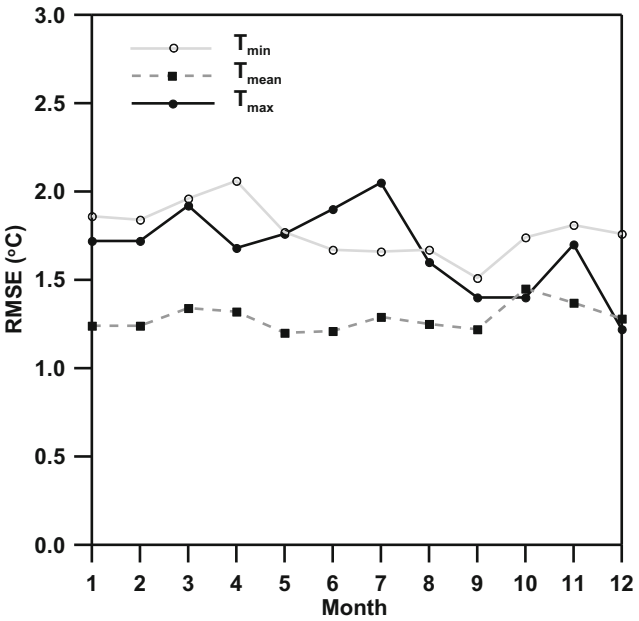

Fig. 8 RMSE for every month

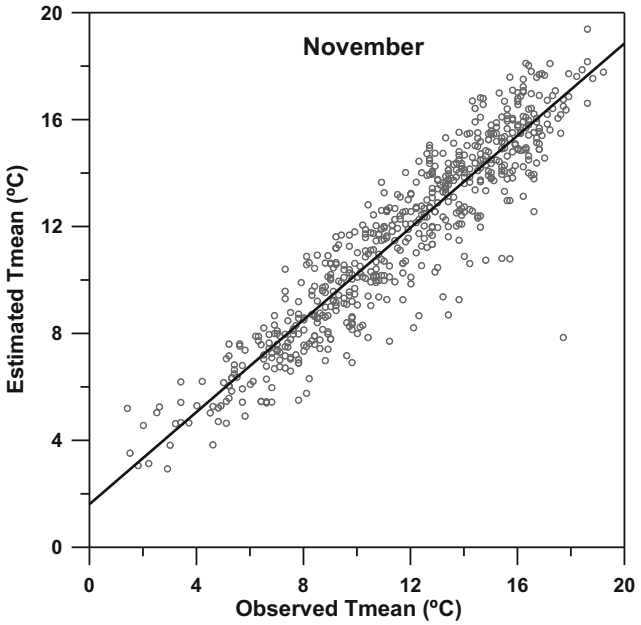

Fig. 9 Estimated versus observed T_{mean} for November

4.4 Discussion of the results

With respect to the correlations among dependent and independent variables used in the multiple regression, it is noticeable, as expected, the high correlation (0.97) between the three daily temperatures (minimum, mean and maximum) and the two LST temperatures and also the calendar day. The correlations are notably small for the rest of independent variables, sometimes achieving values lower to 0.23. Another relevant question is that results obtained by PC analysis, taking into account the thermometric stations or the dense network of 1 km^2 pixels, are very similar. Consequently, the relatively sparse distribution of the 48 thermometric gauges would not be a shortcoming to obtain a reliable spatial distribution of temperatures, being then defined a relatively good image of the thermometric variability on the BMR.

With respect to the multiple linear processes, the square regression coefficients obtained at annual scale are notably good, in spite of the RMSE varies within the (1.5–2.0 °C), results quite similar to those obtained by Cristóbal et al. (2008)

Table 12 Significant variables in decreasing order exceeding Beta equal to 0.20 for the multiple regression process at monthly scale of T_{min}, T_{mean} and T_{max}

Month	T_{min} significant standardised beta coefficients > 0.20
January	lat(− 0.926), lon (0.754), con(0.524), LST_n(0.486), LST_d (0.358), alt(0.254)
February	lat(− 0.723), LST_n(0.690), lon(0.456), con(0.425)
March	LST_n(0.661), LST_d(0.205)
April	LST_n(0.701), lat(− 0.683), lon(0.531), con(0.626)
May	lat(− 0.709), lon(0.686), LST_n(0.361), NDBI(0.231)
June	lat(− 0.564), lon(0.533), LST_n(0.499), NDVI (− 0.242), alt (0.236), cd*(0.231), slp(0.217)
July	lon(0.628), lat(− 0.582), LST_n(0.467), NDVI(− 0.207)
August	lat(− 0.600), lon(0.476), LST_n(0.474)
September	lat(− 0.893), lon(0.835), LST_n(0.439)
October	LST_n(0.690), lat(− 0.569), lon(0.462)
November	lat(− 0.770), LST_n(0.600), lon(0.584), con(0.311), alt(0.270)
December	lat(− 0.598), LST_n(0.531), alt(0.309), NDVI(− 0.238)
Month	T_{mean} significant standardised beta coefficients > 0.20
January	LST_n(0.588), LST_d (0.457), con(0.213)
February	LST_n(0.482), alt(− 0.323),LST_d (0.286)
March	LST_n(0.650), LST_d(0.393)
April	LST_n(0.685)
May	LST_n(0.376),alt(− 0.366), LST_d (0.250), cd*(− 0.202)
June	LST_n(0.451), LST_d (0.409), NDBI(− 0.219)
July	LST_n(0.435), alt(− 0.333), cd*(− 0.318), LST_d (0.208)
August	LST_d(0.358), LST_n (0.282), alt(− 0.273)
September	LST_n(0.369), alt(− 0.377), LST_d (0.265), NDVI(0.212)
October	LST_n(0.629), LST_d (0.219)
November	LST_n(0.645), LST_d (0.223)
December	LST_n(0.577), LST_d (0.271), slp(0.227)
Month	T_{max} significant standardised beta coefficients > 0.20
January	LST_d(0.530), alt(− 0.532), LST_n (0.398), lat(0.484), lon(− 0.309)
February	LST_d(0.557), alt(− 0.547), lat (0.357), lon(− 0.322)
March	LST_d(0.556), LST_n(0.489), con(0.329), alt(− 0.317)
April	alt(− 0.459), lon(− 0.490), LST_n(0.415), lat(0.360), LST_d(0.260)
May	alt(− 0.409), LST_d(0.395), con(0.387), cd*(− 0.313)
June	LST_d(0.510), alt(− 0.422), con (0.330), NDBI(− 0.329)
July	alt(− 0.403), LST_d(0.399), con(0.390), cd*(− 0.347)
August	LST_d(0.535), alt(− 0.468), con (0.243)
September	alt(− 0.604), LST_d(0.456), NDVI(0.364)
October	LST_n(0.503), LST_d(0.363), lon(− 0.345), alt(− 0.329), lat(0.275)
November	LST_n(0.434), LST_d(0.430), alt(− 0.410), alt(− 0.329), lon(− 0.359), lat(0.284)
December	alt(− 0.814), lon(− 0.508), lat(0.481), LSt_d(0.355)

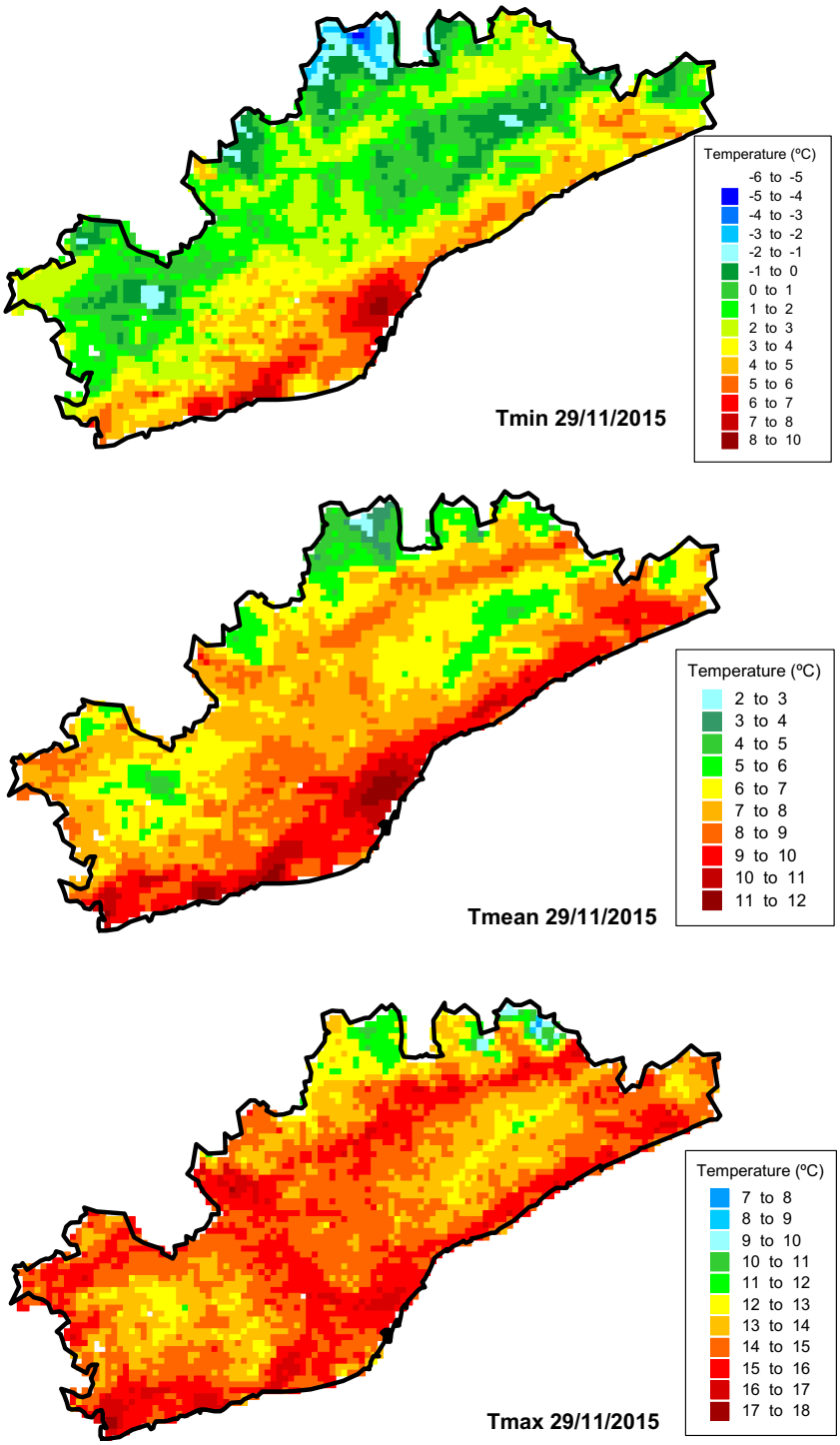

Fig. 10 Example of the spatial distribution of T_{min}, T_{mean} and T_{max} derived by multiple regression for November 29, 2015

for the whole Catalonia. For the results at seasonal and monthly scales, even though the square regression coefficients are lesser than those obtained at an annual scale, the RMSE values are very similar, being not exceeded 2.1 °C. Consequently, the images of the spatial distribution of temperatures should be of similar quality at annual, seasonal and monthly scales. Nevertheless, the highest RMSE values are detected at a monthly scale (T_{min} for April and T_{max} for July).

Another noticeable characteristic is the low weight of NDVI and NDBI on the multiple linear regression, which has been also detected in other similar analysis around the world. In spite of both coefficients could be relevant, as they represent the type of vegetation and building respectively, the LST obtained from satellite data could itself include a great percentage of the information concerning NDVI and NDBI.

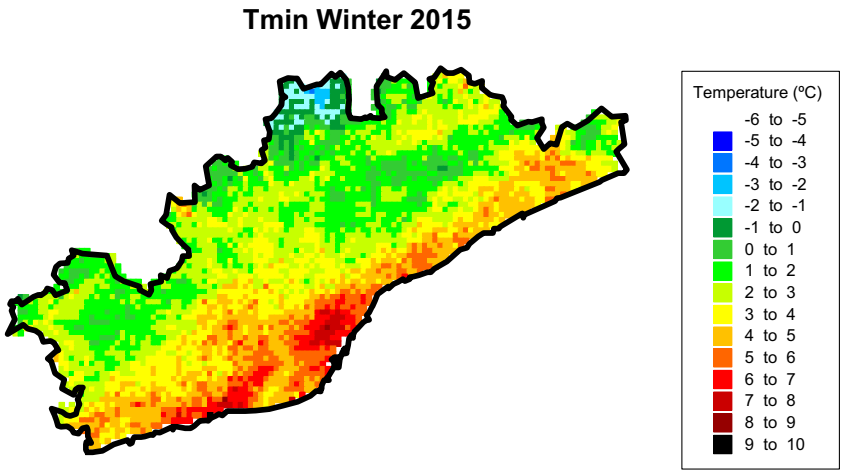

Fig. 11 Winter season spatial distribution of average T_{min} derived by multiple regression

From an applied point of view, given that the obtained thermometric maps are submitted to a maximum RMSE of 2 °C, a dense network of minimum, mean and maximum temperature data could be possible to analyse thermometric phenomena (UHI and hot and cold outbreaks) affecting life quality and health of BMR population. Additionally, data obtained with smaller pixels, for instance with LANDSAT satellite, would permit a notable increase in the spatial resolution of temperatures. Unfortunately, the available data from LANDSAT is nowadays minor than that found from MODIS satellite, and the accuracy of the results would be then questionable.

5 Conclusions

Previous to the multiple regression process, the Pearson correlation coefficient and the PCA have permitted to detect links between empiric temperatures recorded at 48 meteorological stations and satellite data, geographic and topographic data and transformed calendar days. The PCA has also permitted to validate if the set of the thermometric stations are appropriate for a good multiple regression process by comparing RPCs and factor loadings corresponding to 48 stations dataset and 1 km^2 pixel network. In spite of the very different spatial data density for thermometric stations and pixel coverage, a few discrepancies are found with respect to the factor loadings of NDVI and NDBI. In this way, a denser network of thermometric data would improve the role of NDVI and NDBI on the multiple regression. It is also worth mentioning the substitution of the topographic parameter of orientation (Ori) by cos(Ori) and sin(Ori), being detected a slight improvement on the relevance of sin(Ori) when it is used instead of Ori in the multiple regression process.

A revision of the multiple regression analyses results manifests the strong relevance of LST_n for T_{min} and T_{mean} and LST_d for T_{max} at the annual scale, as obtained by Thanh et al. (2016). A similar pattern is observed at a seasonal scale. The relevance at a monthly scale of LST_d on T_{min} is not significant for February, April, May, June and September. Additionally, the relevance of LST_n on T_{max} is not significant for September.

With respect to specific results at the annual scale, first of all, it is noticeable that the best fit between empiric temperatures and those generated by multiple regression is usually found for T_{mean}, being obtained the worst for T_{max} in terms of R^2 and RMSE. It is also noticeable that cd* only plays a relatively important role for T_{min} and the set of relevant variables are not the same for T_{min}, T_{mean} and T_{max}. At monthly scale, whereas the best fits are effectively obtained since January to December for T_{mean}, the worst fit is obtained for T_{max} (June, July) and T_{min} (April). At a seasonal scale, the results are quite different. Whereas the minimum residual for T_{mean} is detected in winter and spring, for T_{min} it is found in summer and for T_{max} in autumn.

In short, the reasonably good results of the multiple regression process would permit:

- Describing with detail (pixels of 1 km^2) the spatial distribution of temperatures, notably improving the spatial data density on BMR derived from the thermometric network and without applying interpolations.
- Obtaining detailed maps of UHI phenomenon on urban areas. It has to be remembered that these details of the UHI intensity could not be obtained from a few thermometric stations. In particular, two clear focus of high UHI intensity for T_{min} in winter have been detected. Additionally, the smooth temperatures along the Mediterranean coast are verified by observing T_{max} and T_{mean} maps.

A systematic and detailed spatial description of temperatures with the methodology used in this paper could be a significant improvement in the analysis of cold and hot outbreaks. It should be underlined that these analyses could be

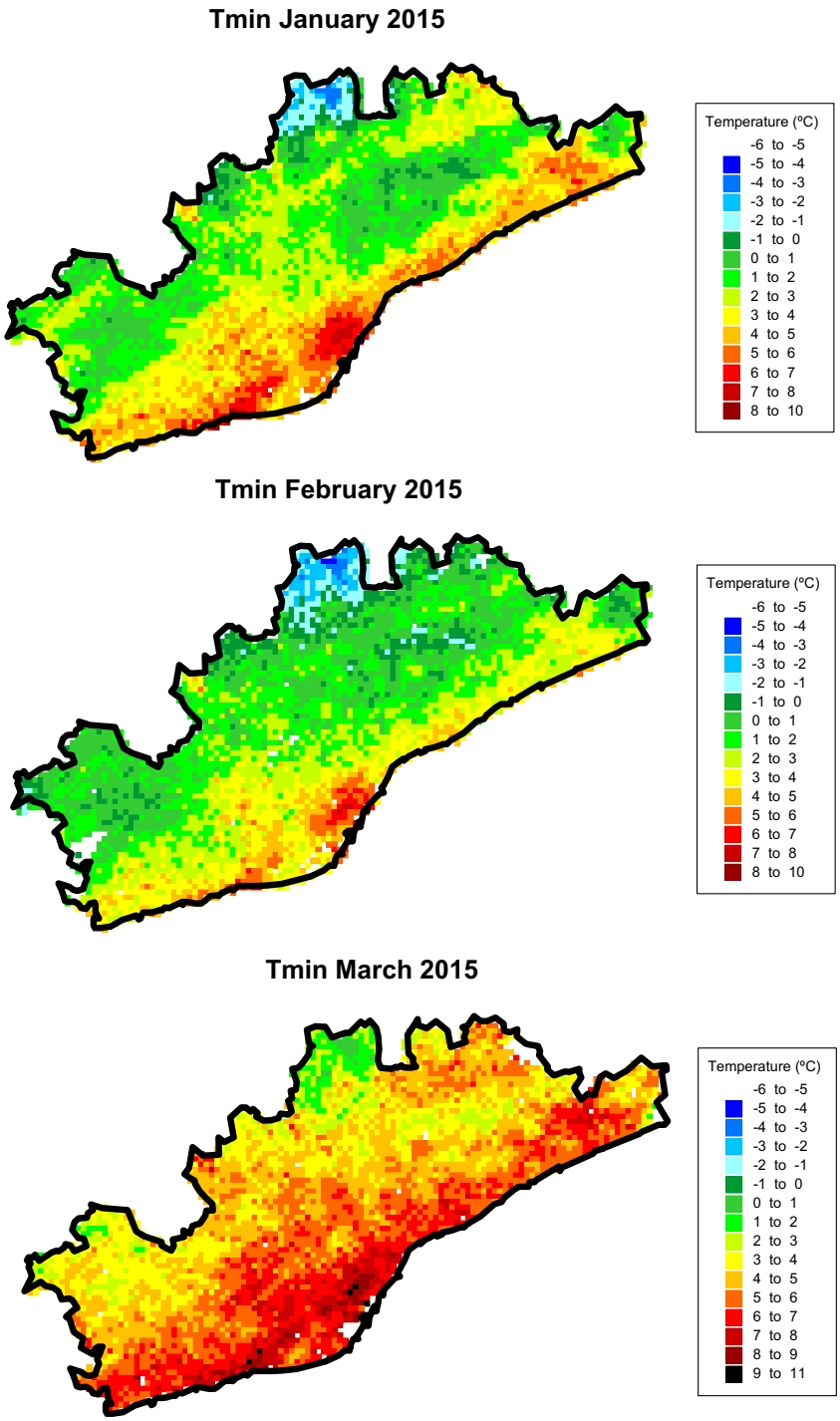

Fig. 12 Monthly spatial distribution (winter season) of average T_{min} derived by multiple regression

very useful to study the effects on the life quality and health of the Barcelona city and metropolitan area inhabitants. Conversely to a relatively scarce distribution of thermometric stations used to analyse these outbreaks, the multiple linear regression method provides a more detailed (1 km × 1 km) spatial distribution of air temperatures.

Finally, comparing R^2 and RMSE for BMR with those obtained by Cristóbal et al. (2008) for the whole Catalonia, it is observed that better results have been obtained for BMR. Whereas for T_{min} and T_{max}, the best results are achieved for BMR (R^2 equal to 0.92 in front of 0.54–0.57 and RMSE equal to 1.5–1.6 °C in front of 2.3–1.8 °C), for T_{mean}, R^2 is again better for BMR (0.96 in front of 0.66). The RMSE for T_{mean} obtained for the whole Catalonia (1.3 °C) is slightly better than that obtained for BMR (1.5 °C). One reason for these differences could be that BMR area is ten times smaller than Catalonia, implying a minor variability of temperatures and geographical characteristics and permitting a better

description of the spatial distribution of temperatures. A higher spatial density of thermometric stations could be another factor favouring the BMR results.

Acknowledgements Temperature data were gently provided by the Agencia Estatal de Meteorología, AEMET, and Servei Meteorològic de Catalunya, SMC.

Funding information This research has been supported by the Spanish Government through the project BIA2015-68623-R (Ministerio de Economía y Competitividad, MINECO and European Regional Development Fund (ERDF).

References

Arnfield AJ (2003) Two decades of urban climate research: a review of turbulence, exchanges of energy and water, and the urban heat island. Int J Climatol 23:1–26

Benali A, Carvalho AC, Nunes JP, Carvalhais N, Santos A (2012) Estimating air surface temperature in Portugal using MODIS LST data. Remote Sens Environ 124:108–121

Buishand TA (1982) Some methods for testing the homogeneity of rainfall records. J Hydrol 58:11–27

Bustos E, Meza FJ (2015) A method to estimate maximum and minimum air temperature using MODIS surface temperature and vegetation data: application to the Maipo Basin, Chile. Theor Appl Climatol 120:211–226. https://doi.org/10.1007/s00704-014-1167-2

Caselles V, Lopez Garcia MJ, Melia J, Perez Cueva AJ (1991) Analysis of the heat-island effect of the city of Valencia, Spain, through air temperature transects and NOAA satellite data. Theor Appl Climatol 43:195–203

Cheval S, Dumitrescu A (2009) The July urban heat island of Bucharest as derived from Modis images. Theor Appl Climatol 96:145–153. https://doi.org/10.1007/s00704-008-0019-3

Cheval S, Dumitrescu A, Bell A (2009) The urban heat island of Bucharest during the extreme high temperatures of July 2007. Theor Appl Climatol 97:391–401. https://doi.org/10.1007/s00704-008-0088-3

Coll C, Caselles V, Galve JM, Valor E, Raquel NR, Sánchez JM, Rivas R (2005) Ground measurements for the validation of land surface temperatures derived from AATSR and MODIS data. Remote Sens Environ 97:288–300

Cresswell MP, Morse AP, Thomson MC, Connor SJ (1999) Estimating surface air temperatures, from Meteosat land surface temperatures, using an empirical solar zenith angle model. Int J Remote Sens 20(6):1125–1132. https://doi.org/10.1080/014311699212885

Cristóbal J, Ninyerola M, Pons X (2008) Modeling air temperature through a combination of remote sensing and GIS data. J Geophys Res 113:D13106. https://doi.org/10.1029/2007JD009318

Dash P, Gottsche FM, Olesen FS, Fischer H (2001) Retrieval of land surface temperature and emissivity from satellite data: physics, theoretical limitations and current methods. J Indian Soc Remote Sens 29:23–30

Dash P, Göttsche FM, Olesen FS, Fischer H (2002) Land surface temperature and emissivity estimation from passive sensor data: theory and practice-current trends. Int J Remote Sens 23(13):2563–2594. https://doi.org/10.1080/01431160110115041

Didari S, Norouzi H, Zand-Parsa S, Khanbilvardi R (2017) Estimation of daily minimum land surface air temperature using MODIS data in southern Iran. Theor Appl Climatol 130:1149–1161. https://doi.org/10.1007/s00704-016-1945-0

Fabrizi R, De Santis A, Gómez A (2011) Satellite und ground based sensors for the urban heat island analysis in the city of Madrid. Joint Urban Remote Sensing Event, Munich, pp 349–352

Fick SE, Hijmans RJ (2017) WorldClim 2: new 1-km spatial resolution climate surfaces for global land areas. Int J Climatol 37:4302–4315

Fu G, Shen Z, Zhang X, Shi P, Zhang Y, Wu J (2011) Estimating air temperature of an alpine meadow on the Northern Tibetan Plateau using MODIS land surface temperature. Acta Ecol Sin 31:8–13

Gallo KP, Tarpley JD, McNab AL, Karl TR (1995) Assessment of urban heat islands: a satellite perspective. Atmos Res 37:37–43

Giannaros TM, Melas D (2012) Study of the urban heat island in a coastal Mediterranean City: the case study of Thessaloniki, Greece. Atmos Res 118:103–120

Good E (2015) Daily minimum and maximum surface air temperatures from geostationary satellite data. J Geophys Res Atmos 120:2306–2324. https://doi.org/10.1002/2014JD022438

Harrell FE (2001) Regression modelling strategies, With applications to linear models, logistic regression models, and survival analysis. Springer, New York, 568 pp

Hengl T, Heuvelink GBM, Percec TM, Pebesma EJ (2012) Spatio-temporal prediction of daily temperatures using time-series of MODIS LST images. Theor Appl Climatol 107:265–277. https://doi.org/10.1007/s00704-011-0464-2

Hung T, Uchihama D, Ochi S, Yasuoka Y (2006) Assessment with satellite data of the urban heat island effects in Asian mega cities. Int J Appl Earth Obs Geoinf 8:34–48

Imhoff ML, Zhang P, Wolfe RE, Bounoua L (2010) Remote sensing of the urban heat island effect across biomes in the continental USA. Remote Sens Environ 114:504–513

Janatian N, Sadeghi M, Sanaeinejad SH, Bakhshian E, Farid A, Hasheminiaa SM, Ghazanfari S (2017) A statistical framework for estimating air temperature using MODIS land surface temperature data. Int J Climatol 37:1181–1194

Jang K, Kang S, Kimball JS, Hong SY (2014) Retrievals of all-weather daily air temperature using MODIS and AMSR-E data. Remote Sens 6:8387–8404. https://doi.org/10.3390/rs6098387

Jin M, Dickinson RE, Zhang DL (2005) The footprint of urban areas on global climate as characterized by MODIS. J Clim 18:1551–1565

Jolliffe IT (1986) Principal component analysis. In: Springer series in statistics. Springer, New York 271 pp

Kilibarda M, Hengl T, Heuvelink GBM, Gräler B, Pebesma E, PercecTadic M, Bajat N (2014) Spatio-temporal interpolation of daily temperatures for global land areas at 1 km resolution. J Geophys Res Atmos 119:2294–2313. https://doi.org/10.1002/2013JD020803

Kloog I, Nordio F, Lepeule J, Andrea PA, Lee M, Auffray A, Schwartz J (2017) Modelling spatio-temporally resolved air temperature across the complex geo-climate area of France using satellite-derived land surface temperature data. Int J Climatol 37:296–304

Landsberg HE (1981) The urban climate. International Geophysics Series, 28. Academic Press, New York 275 pp

Lin S, Moore NJ, Messina JP, DeVisser MH, Wu J (2012) Evaluation of estimating daily maximum and minimum air temperature with MODIS data in east Africa. Int J Appl Earth Obs Geoinf 18:128–140

Lin X, Zhang W, Huang Y, Sun W, Han P, Yu L, Sun F (2016) Empirical estimation of near-surface air temperature in China from MODIS LST data by considering physiographic features. Remote Sens 8:629. https://doi.org/10.3390/rs8080629

Ma W, Zhou L, Zhang H, Zhang Y, Dai X (2016) Air temperature field distribution estimations over a Chinese mega-city using MODIS land surface temperature data: the case of Shanghai. Front Earth Sci 10:38–48. https://doi.org/10.1007/s11707-015-0510-y

Martínez MD, Serra C, Burgueño A, Lana X (2010) Time trends of daily maximum and minimum temperatures in Catalonia (ne Spain) for the period 1975–2004. Int J Climatol 30:267–290

Mendelsohn R, Kurukulasuriya P, Basist A, Kogan F, Williams C (2007) Climate analysis with satellite versus weather station data. Clim Chang 81:71–83. https://doi.org/10.1007/s10584-006-9139-x

Miao S, Chen F, Lemone MA, Tewari M, Li Q, Wang Y (2009) An observational and modeling study of characteristics of urban heat island and boundary layer structures in Beijing. J Appl Meteorol Climatol 48:484–501

Moreno-Garcia MC (1994) Intensity and form of the urban heat island in Barcelona. Int J Climatol 14:705–710

Nemani RR, Running SW (1989) Estimation of regional surface resistance to evapotranspiration from NDVI and thermal IR AVHRR data. J Appl Meteorol 28:276–284

Nieto H, Sandholt I, Aguado I, Chuvieco E, Stisen S (2011) Air temperature estimation with MSG-SEVIRI data: calibration and validation of the TVX algorithm for the Iberian Peninsula. Remote Sens Environ 115:107–116

Peón J, Recondo C, Calleja JF (2014) Improvements in the estimation of daily minimum air temperature in peninsular Spain using MODIS land surface temperature. Int J Remote Sens 35:5148–5166

Pettitt AN (1979) A non-parametric approach to the change-point problem. J Appl Stat 28(2):126–135

Pongrácz R, Bartholy J, Dezsö Z (2006) Remotely sensed thermal information applied to urban climate analysis. Adv Space Res 37:2191–2196

Pongrácz R, Bartholy J, Dezsö Z (2010) Application of remotely sensed thermal information to urban climatology of Central European cities. Phys Chem Earth 35:95–99

Preisendorfer RW (1988) Principal component analysis in meteorology and oceanograph. Elsevier, New York

Prihodko L, Goward SN (1997) Estimation of air temperature sensed surface observations from remotely. Remote Sens Environ 60: 335–346

Rao PK (1972) Remote sensing of urban "heat islands" from an environmental satellite. Bull Am Meteorol Soc 53:647–648

Recondo C, Peón JJ, Zapico E, Pendás E (2013) Empirical models for estimating daily surface water vapour pressure, air temperature, and humidity using MODIS and spatiotemporal variables. Applications to peninsular Spain. Int J Remote Sens 34:8051–8080. https://doi.org/10.1080/01431161.2013.828185

Richman RB (1986) Rotation of principal components. Int J Climatol 6: 293–335. https://doi.org/10.1002/joc.3370060305

Schneider A, Friedl MA, Potere D (2009) A new map of global urban extent from MODIS satellite data. Environ Res Lett 4:044003. https://doi.org/10.1088/1748-9326/4/4/044003

Shah DB, Pandya MR, Trivedi HJ, Jani AR (2013) Estimating minimum and maximum air temperature using MODIS data over Indo-Gangetic Plain. J Earth Syst Sci 122:1593–1605

Shen S, Leptoukh GG (2011) Estimation of surface air temperature over central and eastern Eurasia from MODIS land surface temperature. Environ Res Lett 6:045206

Sohrabinia M, Zawar-Reza P, Rack W (2015) Spatio-temporal analysis of the relationship between LST from MODIS and air temperature in New Zealand. Theor Appl Climatol 119:567–583

Stewart ID (2011) A systematic review and scientific critique of methodology in modern urban heat island literature. Int J Climatol 31:200–217

Sun H, Chen Y, Gong A, Zhao X, Zhan W, Wang M (2014) Estimating mean air temperature using MODIS day and night land surface temperatures. Theor Appl Climatol 118:81–92

Thanh NP, Kappas M, Degener J (2016) Estimating daily maximum and minimum land air surface temperature using MODIS land surface temperature data and ground truth data in northern Vietnam. Remote Sens 8:1002. https://doi.org/10.3390/rs8121002

Tomlinson CJ, Chapman L, Thornes JE, Baker C (2011) Remote sensing land surface temperature for meteorology and climatology: a review. Meteorol Appl 18:296–306

Tomlinson CJ, Chapman L, Thornes JE, Baker CJ, Prieto-Lopez T (2012) Comparing night-time satellite land surface temperature from MODIS and ground measured air temperature across a conurbation. Remote Sens Lett 3:657–666. https://doi.org/10.1080/01431161.2012.659354

Vancutsem C, Ceccato P, Dinku T, Connor SJ (2010) Evaluation of MODIS land surface temperature data to estimate air temperature in different ecosystems over Africa. Remote Sens Environ 114:449–465

Voogt JA, Oke TR (2003) Thermal remote sensing of urban climates. Remote Sens Environ 86:370–384

Wan ZM, Zhang YL, Zhang QC, Li ZL (2002) Validation of the land-surface temperature products retrieved from Terra Moderate Resolution Imaging Spectroradiometer data. Remote Sens Environ 83:163–180

Wan Z, Wang P, Li X (2004) Using MODIS land surface temperature and normalized difference vegetation index products for monitoring drought in the southern Great Plains, USA. Int J Remote Sens 25(1):61–72

Wang W, Liang S, Meyers T (2008) Validating MODIS land surface temperature products using long-term nighttime ground measurements. Remote Sens Environ 112:623–635

Wang L, Koike T, Yang K, Yeh PJF (2009) Assessment of a distributed biosphere hydrological model against streamflow and MODIS land surface temperature in the upper Tone River Basin. J Hydrol 377: 21–34

Wenbin Z, Aifeng L, Shaofeng J (2013) Estimation of daily maximum and minimum air temperature using MODIS land surface temperature products. Remote Sens Environ 130:62–73

Wijngaard JB, Klein Tank MG, Können GP (2003) Homogeneity of 20th century European daily temperature and precipitation series. Int J Climatol 23:679–692

Williamson SN, Hik DS, Gamon JA, Kavanaugh JL, Koh S (2013) Evaluating cloud contamination in clear-sky MODIS Terra daytime land surface temperatures using ground-based meteorology station observations. J Clim 26:1551–1560

Xu Y, Knudby A, Ho HC (2014) Estimating daily maximum air temperature from MODIS in British Columbia, Canada. Int J Remote Sens 35:8108–8121. https://doi.org/10.1080/01431161.2014.978957

Yang P, Ren G, Liu W (2013) Spatial and temporal characteristics of Beijing urban heat island intensity. J Appl Meteorol Climatol 52: 1803–1816

Yang YZ, Cai WH, Yang J (2017) Evaluation of MODIS land surface temperature data to estimate near-surface air temperature in Northeast China. Remote Sens 9:410. https://doi.org/10.3390/rs9050410

Yasuoka Y (2006) Assessment with satellite data of the urban heat island effects in Asian mega cities. Int J Appl Earth Obs Geoinf 8:34–48

Zaksek K, Schroedter-Homscheidt M (2009) Parameterization of air temperature in high temporal and spatial resolution from a combination of the SEVIRI and MODIS instruments. ISPRS J Photogramm Remote Sens 64(4):414–421

Zhang X, Friedl MA, Schaaf CB, Strahler AH, Hodges JCF, Gao F, Reed BC, Huete A (2003) Monitoring vegetation phenology using MODIS. Remote Sens Environ 84(3):471–475

Zhang W, Huang Y, Yu Y, Sun W (2011) Empirical models for estimating daily maximum, minimum and mean air temperatures with MODIS land surface temperatures. Int J Remote Sens 32(24):9415–9440. https://doi.org/10.1080/01431161.2011.560622